CHAPTER 18

THz Investigations of Condensed Phase Biomolecular Systems

Hailiang Zhang,[⋆] Karen Siegrist,[†] Kevin O. Douglas,[‡] Susan K. Gregurick,[⋆] and David F. Plusquellic[‡]

[⋆]Department of Chemistry and Biochemistry
University of Maryland
Baltimore County
Baltimore, Maryland 21250.

[†]Electro-optical and Infrared Systems and Technologies Group
Johns Hopkins Applied Physics Laboratory
Laurel, Maryland 20723

[‡]Biophysics Group
Physics Lab, National Institute of Standards and Technology
Gaithersburg, Maryland 20899-8443

Abstract

Terahertz (THz) spectroscopic investigations of crystalline dipeptide nanotubes are discussed in the frequency region from 0.6 (2 cm^{-1}) to 3 THz (100 cm^{-1}). The THz region provides access to collective modes of biomolecular systems and is therefore sensitive to the large scale motions important for understanding the impact of environmental stimuli in biomolecular systems. The focus of this chapter is on THz spectral changes observed in this region when crystals of alanyl isoleucine (AI) and isoleucyl alanine (IA) nanotubes are exposed to water. Of biological

0091-679X/08 $35.00
DOI: 10.1016/S0091-679X(08)00818-2

significance is the water permeability through hydrophobic pore regions as exemplified in the disparate behavior of these two dipeptide nanotubes. AI is known from X-ray studies and confirmed here to act reversibly to the exchange of water while IA does not accept water into its pore region. Both quantum chemical and classical calculations are performed to better understand the subtle balance that determines guest molecule absorption and conduction through these hydrophobic channels. Examination of the vibrational character of the THz modes with and without water suggests water mode coupling/decoupling with collective modes of the nanotube may play an important role in the permeability dynamics.

I. Introduction

Water is ubiquitous in biological systems. Biomolecular interactions with water are vital to facilitating conformational changes, and to cellular transport through membrane pores, processes which rely on the concerted motions, and interactions of many atoms or molecules. Water transport through membranes has itself been a topic of much interest, since the first structural determination of a membrane channel, the water-selective aquaporin AQP1 (Preston *et al.*, 1992). Further investigation of membrane transport processes has proceeded at a rapid rate. Such processes are highly sensitive to the delicate balance in chemical potentials between hydrophilic (hydrogen bonding) and hydrophobic interactions with water. Terahertz (THz) vibrational modes, involving the same types of nonlocal and collective motions relevant to such processes, are similarly sensitive to hydrogen bonding and hydrophobic interactions with water. Here, we demonstrate the THz spectral sensitivity of small biomolecules to the presence or absence of water, and in particular, to the interactions of water with pore-forming crystalline dipeptides having vastly different water permeability.

THz spectroscopy is a natural tool for probing the mechanisms important to biological function. The characteristic modes found in this low energy spectral region correspond to collective motions of many atoms or molecules that extend over the nanometer length scale. In contrast to the localized motions of two or three atoms probed in the higher frequency infrared region (typically carbonyl and amide stretching or bending modes), THz modes are exemplified by the tail-wagging and backbone-bending motions intrinsic to the conformational changes and the collective motions of many biological processes. Recent work in this rapidly growing field has proven its potential for unraveling picosecond dynamics of biomolecular interactions (Ebbinghaus *et al*., 2007, 2008; Heugen *et al.*, 2006; Heyden *et al.*, 2008), identifying conformations (Whitmire *et al*, 2003) and imaging biological processes (Masson *et al*., 2006). In much of this recent work, the high sensitivity of the THz response to the interactions of biological molecules with water has been demonstrated. For example, probing the picosecond dynamics occurring at THz frequencies has revealed a dynamical hydration shell that extends out to 5 Å from the surface of lactose (Heugen *et al.*, 2006), even further for trehalose (Heyden *et al.*, 2008), and as far as 10 Å from protein surfaces

(Ebbinghaus *et al*., 2007). These dynamics are unveiled by variations in the THz dielectric response to additional solvation layers, thus demonstrating the qualitative difference in bulk water versus biological water at THz frequencies, as well as the surprisingly long range effects of biomolecules on surrounding water. This verification of the differential dielectric response of hydration shells versus bulk water supports previous predictions from molecular dynamics (MD) simulations of water confined in pores (Sansom *et al*., 1997). These investigations give credibility to the usefulness of THz spectroscopy for investigating interactions of biomolecules with water.

In much of the recent work directed at developing a theoretical understanding of THz vibrational modes of biomolecules, crystalline solids have been investigated. The highly degenerate vibrational modes of small crystalline systems can often give rise to sparse and well-resolved spectral features providing benchmark data ideally suited for development and validation of theoretical models. To this end, much progress has been demonstrated in reproducing the experimentally observed THz vibrational spectra for biomolecular crystalline systems (Allis *et al*., 2007; Jepsen and Clark, 2007; Siegrist *et al*., 2006).

In initial work, the alanine tripeptide gives striking evidence of the impact of hydrogen-bonded water on the THz spectra of the crystalline solids (Siegrist *et al*., 2006). In the present work, our focus is on the effect of hydration on the THz spectra of two hydrophobic dipeptide nanotubes, L-alanyl-L-isoleucine (AI) and L-isoleucyl-L-alanine (IA). These two pore-forming peptides belong to a seven-member family of dipeptide nanotubes which share the same hexagonally symmetric crystal structure, but have different pore diameters and different solvation characteristics. Of this pair, AI is known to absorb water molecules, whereas IA does not take up water (Gorbitz, 2003). Structural modeling at the quantum chemical (density functional theory) and empirical force field levels are used to gain understanding of the mechanisms impacting the permeability of the dipeptide pores to water.

For pores of small diameter, MD simulations have shown that water molecules can permeate small hydrophobic pores by forming highly correlated single chains threading down the nanotube (Allen *et al*., 1999). MD simulations have indicated that permeability of membrane pores to water (or other ions) depends upon a critical pore radius, but a number of factors other than geometry can influence the critical radius for permeability, so that a pore may not be physically occluded yet nonetheless impermeable to certain solvents (Beckstein and Sansom, 2004). In particular, perturbations in pore wall polarity can induce large changes in critical pore radius and thus impact transport (Beckstein and Sansom, 2004; Hummer *et al*., 2001). In MD simulations of the aquaporin channel AQP1, De Groot and Grubmuller (2001) attribute high rates of water transmission through the hydrophobic pore to collective motions of the intrapore water. Similarly, Hummer and coworkers (2001) report pulse-like transmission of water through hydrophobic carbon nanotubes, while the work of Pomes and Roux (1998) implies that collective motions are needed to sustain proton conduction along intrapore water chains. We suggest that THz vibrational mode couplings of the pore wall to the intrapore

water can drive the collective motions that may be necessary for water (or proton) transmission through nanoscale pores. The results of structural modeling of these simple dipeptide nanotubes further suggests that the character of the low frequency THz modes can bear on the ability of pores to admit or exclude solvent molecules, via the picosecond timescale dipole coupling which can impact the critical radius for permeability, as well as affect the physical diameter of the pore.

The simplified pore model described by Lynden-Bell and Rasaiah (1996) can provide an intuitive basis for relating the collective nature of THz modes to the process of water transport. This extremely simple model treats the pore as an infinite cylinder with a very steep wall potential. Within the radially symmetric charge distribution we imagine giving rise to this potential, no electrostatic radial field can exist, although variations along the pore axis can give rise to electrostatic axial fields. Perturbations of such a system, however, clearly can give rise to periodic fields which can be visualized as similar to the allowed modes of a cylindrical waveguide. Such fields involve periodic axial and radial constriction forces, as well as torsional forces which can periodically twist or kink the tube, and can be expected to couple to the current provided by a central water chain, possibly driving transmission. Our structural modeling in fact shows the existence of pore "breathing" modes, for these model nanotubes (Zhang *et al.*, 2008). In these THz frequency "breathing" modes, the pore alternately constricts and relaxes, its inner diameter visibly changing throughout the vibration. This result is suggestive that the character of low frequency nonlocal THz modes of nanopores can impact pore permeability. We will discuss the impact of water–biomolecule interactions on THz spectra of small peptides, using structural modeling to understand the nature and functional impact of THz modes.

II. Instrumentation

The continuous wave THz spectrometer used in these studies has been described in detail elsewhere (Korter and Plusquellic, 2004; Pine *et al.*, 1996; Plusquellic *et al.*, 2003). Briefly, the system shown in Fig. 1 consists of a GaAs photomixer (McIntosh *et al.*, 1995; Verghese *et al.*, 2001) as the source of THz radiation, a liquid He-cooled (LHe) sample assembly and a LHe bolometer detector. The photomixer is driven at the difference frequency of two infrared lasers. Output from a fixed frequency laser at 840 nm is combined with that from a grating-tuned standing wave cavity Ti:Sapphire laser having a resolution of $\approx$0.04 cm^{-1} (1.2 GHz). The two collinear beams are focused onto the photomixer to produce the THz radiation at the difference frequency. Tuning of the Ti:Sapphire laser is achieved over the range (0–3) THz (0–100 cm^{-1}) by stepper-controlled grating. A maximum power estimated at 5 μW is obtained near 0.6 THz (20 cm^{-1}). The THz source, sample, and detector are enclosed in a vacuum chamber to permit LHe sample temperatures ($\approx$4 K) to be reached and to avoid absorption by atmospheric water–vapor. The THz beam is collimated by a silicon lens and then

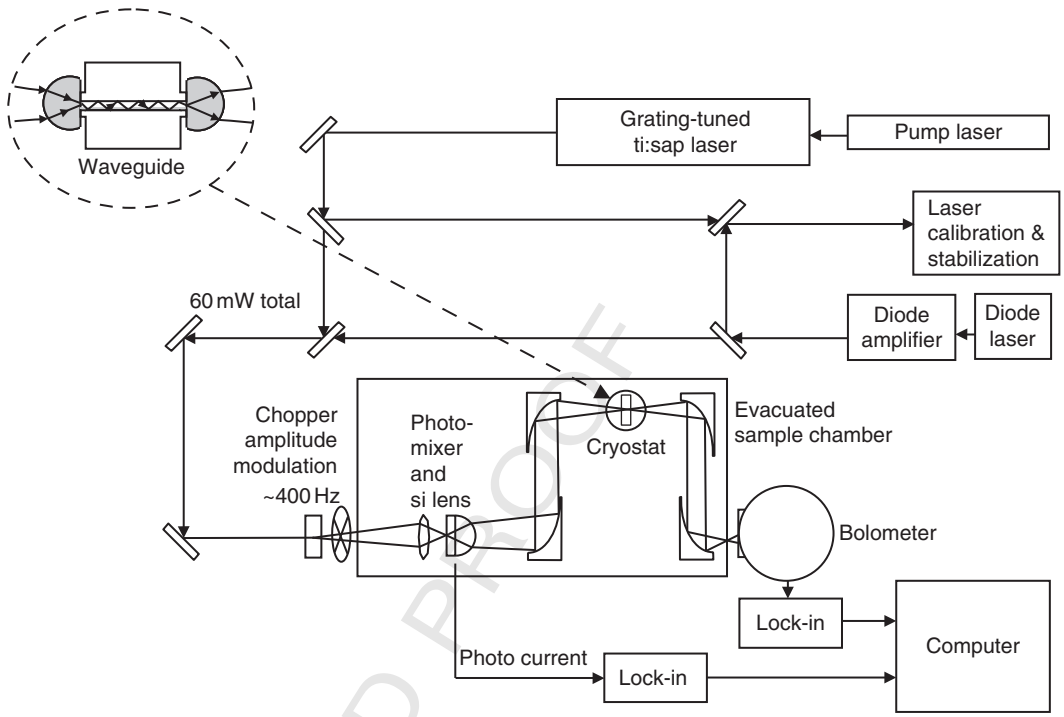

Fig. 1 Schematic of the continuous wave THz spectrometer. The sample is placed in a holder on the cold finger of the cryostat. For thin film samples, the parallel plate waveguide assembly shown in the inset replaces the standard sample holder.

focused by off-axis parabolic mirrors onto the sample fixed to the cold finger of a cryostat and then onto a LHe silicon composite bolometer having a power detection sensitivity of <1 nW up to 3 THz in a 400 Hz bandpass (Noise Equivalent Power of the bolometer is 1 pW/Hz$^{1/2}$). The photocurrent of the photomixer is simultaneously recorded with absorption to correct changes in laser powers at the photomixer.

For scans performed on bulk sample pellets, the crystalline peptides obtained directly from Bachem (see disclaimer) at $>99\%$ purity were diluted with fine grain polyethylene (PE) powder (average particle diameter 4 μm), and 100 mg of a 10%–15% concentration mixture were pressed at 2×10^7 Pa (3000 psi) to form a disk $\sim$750 μm thick and 13 mm in diameter. This disk was placed in a brass holder attached to the cryostat coldfinger. A pure PE pellet sample was also prepared to obtain the power transmission spectra for rationing purposes.

THz experiments using a plane-parallel waveguide (Melinger *et al.*, 2006, 2007; Mendis and Grischkowsky, 2001) required a modification of the sample system. The inset of Fig. 1 shows the plane-parallel waveguide assembly, fabricated of copper for high thermal conductivity and coated with gold to minimize surface reactivity. The waveguide path length of 2.5 cm was chosen to enable the assembly

to be mounted inside of the cryostat heat shield. Hyper-hemicylindrical silicon lenses couple the THz radiation into and out of the waveguide. The lenses have a diameter of 12 mm and a shoulder offset to place the focal point at the flat silicon surface. A small ($\approx$50 μm) gap exists between the lens and the waveguide. A thin film of the crystalline dipeptide was prepared on the upper removable plate of the waveguide. Acetone was added to a nearly saturated aqueous solution of dipeptide to aid the wetting of the gold surface (which is prone to induce hydrophobic beading of the solution). A few hundred microliters of solution were drop cast on the gold surface and evaporated at 75–80 °C. A uniform crystalline film, composed of a patchwork of oriented crystallites, provided visual confirmation of the successful deposition of sample. The quantity of sample was determined to give optimal signals between 10% and 90% fractional absorption. Based on this quantity, the dipeptide films are estimated to be 1–2 μm thick.

The waveguide assembly was fixed to the cold finger of the cryostat and inserted into the beam path at nearly the same position occupied by the sample holder in prior experiments. For our incompletely optimized system, only minor adjustments were made to the THz beam collimation to improve coupling into the waveguide. A waveguide plate separation of 250 μm was maintained using Teflon spacers at the edges of the 3.75 cm (1.5 in.) wide assembly and this rather large gap gave sufficient sensitivity for the $\sim$1 mg of dipeptide film. Fine adjustment of these short focal length lenses is necessary to achieve good parallel alignment with the gap at the correct vertical position. The assembly allows adjustment via set screws. A place-holding bracket was then locked in place to fix the correct lens position, which allowed disassembly and reassembly of the waveguide without losing lens alignment. An additional positioning system was used to improve the stability and repeatability of the cryostat position in the beam path.

During acquisition of spectra, the helium-cooled sample assembly was held at 4.2 K in vacuum for the PE-diluted disk-shaped samples in the smaller brass assembly. The larger gold-coated copper waveguide assembly was held at 4.6 K, the minimum temperature which could be achieved due to the necessary removal of one radiation shield. It is possible that the temperature of the sample is higher than the readout indicates, since the thermistor is placed at the base of the cold finger, and not at the sample location. However, since the temperature is not observed to rise immediately after cessation of helium flow, it is assumed to be within 1 K of the nominal 4.6 K indicated on the control box.

III. Theory

An overview of the computational methods used to model some of the THz spectra presented here has been given elsewhere (Plusquellic *et al.*, 2007). Quantum chemical calculations were performed using density functional theory (DFT) as implemented in the software suite, DMol^3 (Delley, 1990, 2000). Periodic boundary conditions were enforced for all crystalline systems. The PW91 exchange

correlation functional based on the generalized gradient approximation (GGA) in the parameterization of Perdew and Wang (1992) was chosen for these studies. A double numerical plus polarization atomic orbital basis set (equivalent to double-ζ) was used and all electrons were included in the calculations. The minimum-energy geometry was optimized with a convergence criteria of 1×10^{-6} hartrees (Ha) for energy, 2×10^{-4} Ha/Å for the maximum gradient, and 5×10^{-4} Å for maximum displacement, and with the atomic orbital cutoff for integration set at the default value, $R_c = 3.7$ Å. All the DMol^3 calculations were performed on unit cell dimensions determined from X-ray crystallographic data and for the dipeptide nanotubes, hexagonal space group symmetry was preserved throughout. Harmonic frequencies and normal-mode displacements were obtained at the Γ-point by a two-point numerical differentiation of the forces, following diagonalization of the mass-weighted Hessian matrix (Wilson *et al.*, 1955) of the unit cell. These conditions were similar to those previously for predicting the THz spectra of trialanine (Siegrist *et al.*, 2006).

In addition to the DFT calculations, empirical force-field calculations were done using periodic boundary conditions in CHARMM22 (MacKerell *et al.*, 1998a,b, 2000). Periodic structures were created using the CRYSTAL facility in the CHARMM-c32b2 package (Brooks *et al.*, 1983) to include a set of image cells surrounding a core block of one unit cell. The core atom cut off radius for including pairwise nonbonded interactions, which determines the number of image cells generated, was set at 20 Å; changes in energy were negligible for larger cut off radii. Inclusion of three-atom hydrogen bonding terms to model interactions between core and image cells are not currently possible. Therefore, all intermolecular hydrogen bonds are treated with two-atom terms. The Ewald approximation (Ewald, 1921) was used to ensure convergence in the electrostatic energy sums, and a Gaussian width of 0.34 cm^{-1} was used in transitioning from real to k-space sums. The number of grid points in k-space was set to approximately twice the unit-cell dimensions. Normal mode frequencies were found from the eigenvalues of the mass-weighted Hessian matrix using a two-point finite difference method. Simulated Gaussian lineshape functions of 1 cm^{-1} in width were convoluted with all predicted spectral lines used for comparison of experimental and computational spectra.

IV. Dipeptides Nanotubes

The crystalline structures of a series of dipeptides have recently been reported by Görbitz (2002, 2003) and Gorbitz and Gundersen (1996). The dipeptide pairs of this structural class, the VA group, have hexagonal space group structures ($P6_1$ Hermann Mauguin space group) and have crystalline structures similar to that shown in Fig. 2A for AI. Other members of this group include alanyl valine (AV), AI, and valyl isoleucine (VI) and their retroanalogs, valyl alanine (VA), IA, and isoleucyl valine (IV). A key property of this class is the hydrophobic surface that

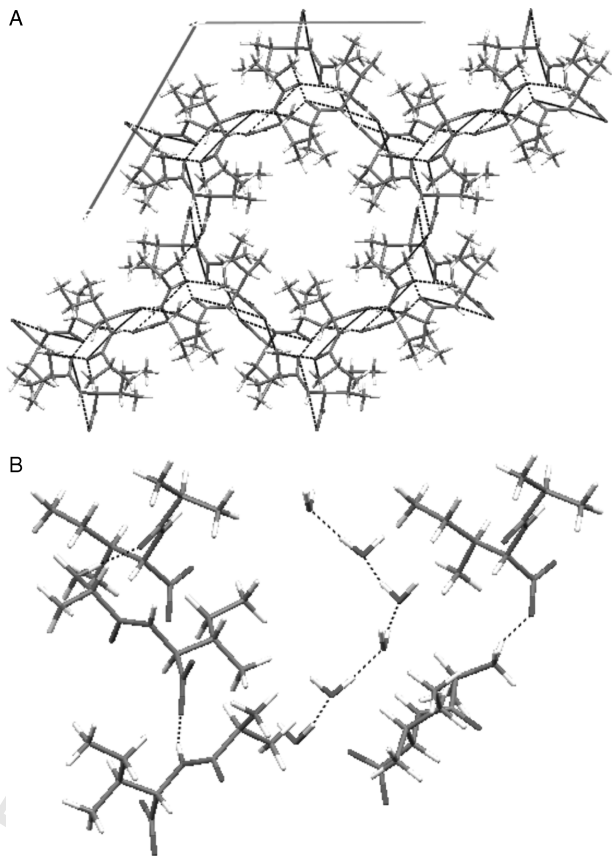

Fig. 2 Crystalline structure of the dipeptide AI (Görbitz and Gundersen, 1996). Top panel illustrates the structure as viewed down the 6_1 axis. The structure of AI–H_2O (1:1 ratio) is shown in the lower panel along an axis perpendicular to the 6_1 axis. Hydrogen bonds are shown with dashed lines. The hydrogen atom positions of water were determined from Density Functional Theory (DFT) predictions (see text for details).

forms the inner lining of the nanotube channels where the side chains are seen to cluster around the hexagonal axis, $\mathbf{6_1}$. The framework of each channel constitutes a double helix that is linked by consecutive $-NH_3^{+\cdots-}OOC-$ head-to-tail hydrogen bonds.

The van der Waals pore diameters of the nanotubes have been found to range from 0.33 to 0.6 nm over this series. For several of these nanotube structures, Görbitz and Gundersen (1996) and Görbitz (2002, 2003) were also able to obtain X-ray data of systems where the pore regions contained hydrophilic solvents such as H_2O, isopropanol, acetone, acetonitrile, and so on. Of particular interest here is the retro-analog pair, AI and IA, where in the former case, the guest solvent, water, was found to be easily drawn into the pores while in the latter case, permeation of water was prohibited. A cross-sectional view of the $\mathbf{6_1}$ structure of AI containing

water in a 1:1 ratio within the pore is shown in Fig. 2B. Like the helical structure of the nano-tubes, the water network takes the form of a spiral with each water molecule binding to its neighbors with two hydrogen bonds (H-bonds). Because of the hydrophobic nature of the tube, the water network is expected to be essentially noninteracting with the network of peptide backbone H-bonds that defines the shape of the nano-tubes. The corresponding pore size changes from 6×4.5 Å in AI to 5×2.5 Å in IA.

The THz absorption spectra obtained at 4 K for bulk (pellet) samples of AI and IA are shown as the middle traces in the upper and lower panels of Fig. 3, respectively. Simulated spectra are superimposed on top of the experimental data traces. The simulations were obtained by fitting the data to a minimum number of Gaussian features to give a quantitative measure of the phonon mode count across this region. Notice the differences in these spectra upon simple reversal of the sequence. The spectrum of AI has more than twice the number of lines as IA. The corresponding spectra of hydrated samples are shown as the upper traces in each panel of Fig. 3. These spectra were obtained shortly after these samples were recrystallized from H_2O according to the prescription given by Gorbitz (Görbitz and Gundersen, 1996) while the lower traces were obtained for samples dried in vacuum for several days following recrystallization. It is clear in the lower panel that little change occurs between the spectra of IA and IA–H_2O. However, while the overall patterns of the two spectra of AI and AI–H_2O are quite similar, features of the hydrated sample are shifted to lower frequency by upto 2.5 cm^{-1} and all features display some added width. The changes are reproducible and easily verified at the resolution of our spectrometer. These studies further confirm the vastly different water permeability dynamics of the two nanotube structures. We further note that this property of AI is in sharp contrast to the absorption of H_2O in alanine tripeptide where significant changes in the THz absorption spectrum were observed for the antiparallel sheet (Seigrist *et al.*, 2006).

The corresponding THz spectra of thin film samples of AI and IA deposited on one surface of a waveguide are shown as the lowest trace in each panel in Fig. 3. The thin films are estimated to be (1–2) μm thick. Furthermore, the thin films were placed under vacuum prior to cooling and data collection and therefore have no water in the nanotubes. Similar to the advantages realized for polymers (Melinger *et al.,* 2006, 2007), the waveguide spectra were obtained with ≈10-fold less sample compared to the bulk pellet spectra and the spectral lines are significantly reduced in width and nearly completely resolved. Furthermore, the vibrational lines are well-aligned with corresponding features in the bulk samples. However, for some lines, the spectral intensities are very different from their bulk sample counterparts. This is a result of selective absorption between the well-aligned polarization supported in the waveguide and orientated crystal growth pattern on the waveguide interface, a property that will be exploited in future studies to elucidate the types of nuclear motions associated with the THz features (Melinger *et al.*, 2007). Like the bulk sample spectra, all features are well-fit to Gaussian lineshape functions indicating that contributions to the spectral widths are due to crystal defects

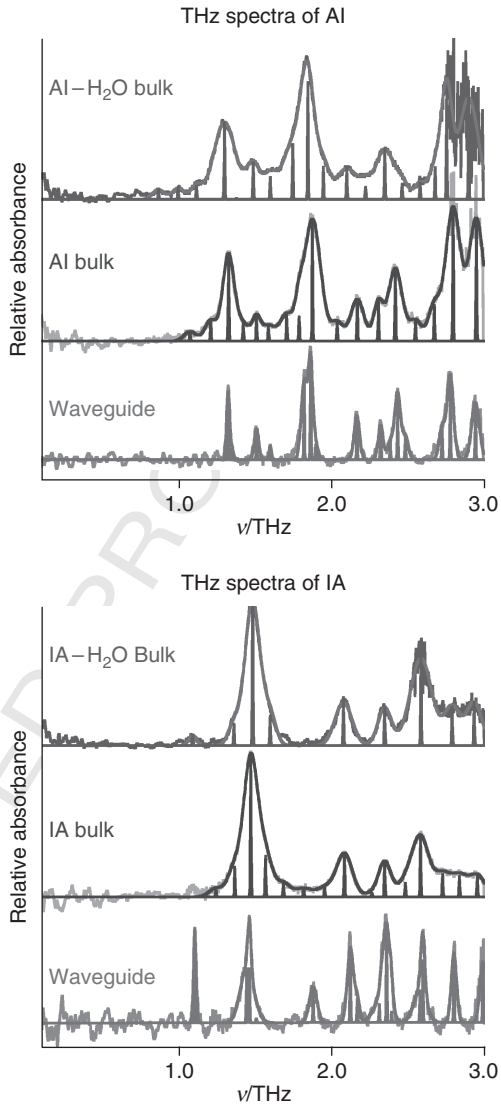

Fig. 3 THz spectra of crystalline samples of AI (top) and IA (bottom). The middle trace in each panel was obtained for samples dried under vacuum for several days while the upper traces were obtained for samples cooled to 4 K immediately following recrystallization from the solvent, water. While the two spectra of IA are nearly identical, the features of AI–H_2O are shifted to the red by $\approx$2.5 cm^{-1} relative to AI. The bottom traces in each trace are from dry samples deposited in a waveguide. Spectra are shifted along the absorbance axis for clarity.

and/or surface anomalies. Such broadening properties keep open the possibility of still further improvements in spectral fidelity.

To gain some understanding of why water behaves so differently in these two dipeptide nanotubes, a series of classical (CHARMM) and quantum chemical calculations (DFT/PW91) were performed on periodic structures with and without water. For these calculations, the unit cell dimensions were held fixed at those determined in the X-ray studies and full geometry optimizations were performed on the *P 61* unit cells with and without water. For AI, the initial positions of the oxygen atoms were taken from the X-ray data while for IA, the initial water network was taken from the optimized geometry of AI. The full optimized structures of the water helices after removal of the dipeptide nanotubes were also performed for each of the *P 61* structures. In these cases, the water networks retained their same three dimensional helical structures.

The THz spectral predictions from CHARMM for AI and IA are shown as the top two traces in the upper and lower panels of Fig. 4, respectively. For both AI and IA without water, the predicted spectra have the correct number of features although the overall patterns of both are rather severely red-shifted relative to experiment. We demonstrate in recent work (Zhang *et al.*, 2008) that predictions from CHARMM improved significantly for seven different nanotube structures (including AI and IA) when anharmonic effects are taken into account using vibrational self-consistent theory (VSCF) (Gregurick *et al.*, 1997, 1999, 2002). In line with the observed features, the VSCF vibrational frequencies blue-shift relative to the harmonic frequencies shown in Fig. 4. These shifts are attributed to the overall positive coupling strengths from a stiffening of the effective potential particularly for the sidechain squeezing modes. Shown as the top traces in each panel of Fig. 4 are the calculated spectra for the hydrated nanotubes. Particularly for AI, the overall pattern of lines is very different from that of the dry nanotubes. Furthermore, the main features seem to show a slight tendency to blue-shift. Both of these properties are inconsistent with observed spectra where the overall pattern of AI–H_2O is very similar except for a small red-shift relative to AI (see Fig. 3).

The THz spectral predictions from quantum chemical theory (DFT) for AI and IA are shown as the top two traces in the upper and lower panels of Fig. 5, respectively. The experimental data of the dehydrated pellet and waveguide samples are shown as the lower two traces for comparison. The optimized theoretical structures are shown in Fig. 6. Except for a small red-shift, the theoretical spectrum of AI is in good agreement with experiment, reproducing nearly all experimental features up through 3 THz. The agreement with the predicted spectrum of IA is also good except for a small blue-shift from theory. Furthermore, in the top panel, the calculated spectrum of the hydrated form, AI–H_2O, is similar to that of AI except for a small uniform red-shift. This property seems to reproduce the experimental observations in Fig. 3. In contrast, the corresponding simulated spectrum of IA–H_2O appears much more complex relative to IA with additional features predicted throughout this region. Examination of the ''extra'' normal modes associated with IA–H_2O indicates a higher propensity for the water motion relative

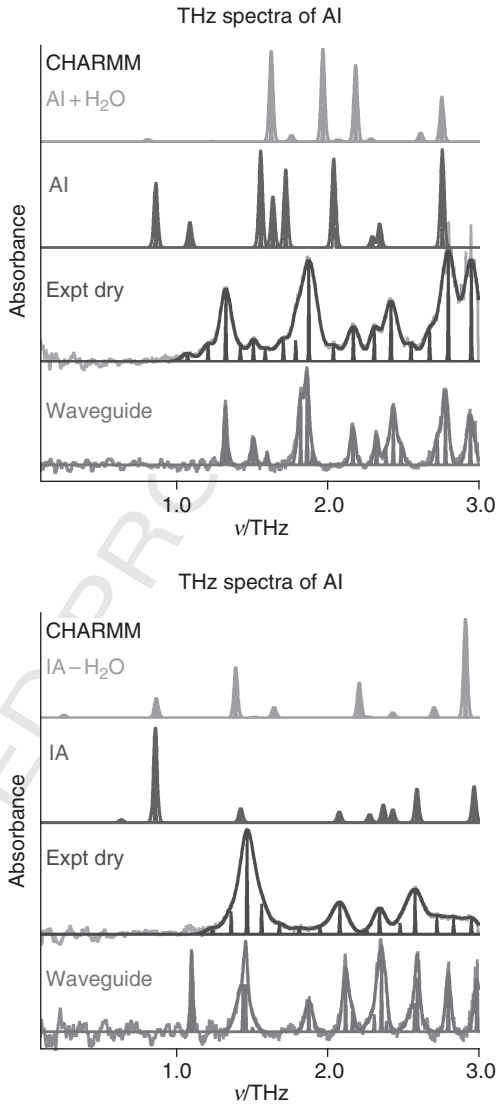

Fig. 4 Spectral predictions of AI (top) and IA (bottom) from CHARMM and the TIP3P Water model. The predicted spectrum shown as the top trace in each panel is for the nanotube structure that includes the helical network of water in the pores. The experimental data of the bulk and waveguide samples are shown below for comparison. Spectra are shifted along the absorbance axis for clarity.

to other modes in this region. In contrast, the relative displacements of water for AI–H_2O appear to be more uniform over all of the THz modes. Hence, the water fluctuations in IA–H_2O appear to be decoupled from those of the nanotube frame. From the thermodynamics perspective, such a decoupling may lead to an increase

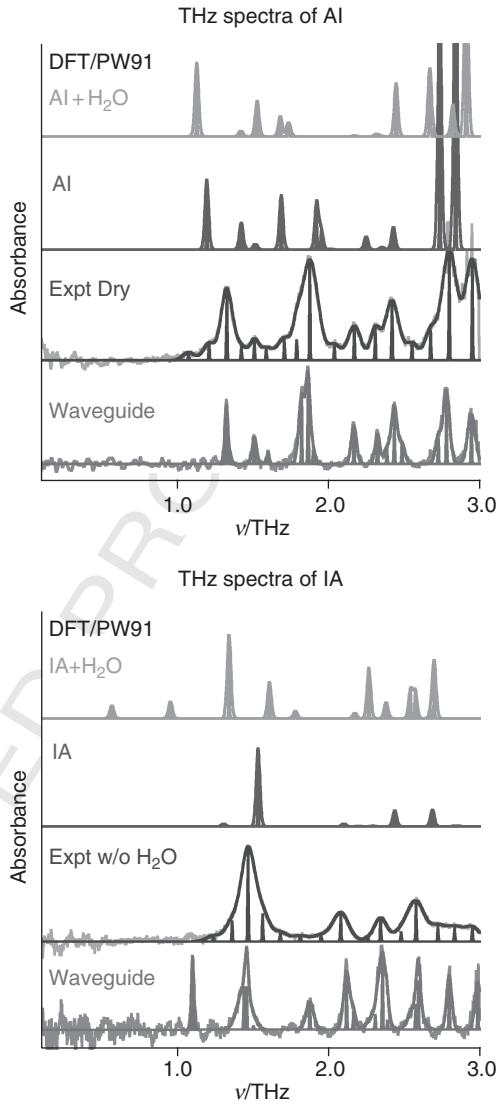

Fig. 5 Spectral predictions of AI (top) and IA (bottom) from DFT and the PW91 functional. The predicted spectrum shown as the top trace in each panel is for the nanotube structure that includes the helical network of water in the pores. The experimental data of the bulk and waveguide samples are shown below for comparison. Spectra are shifted along the absorbance axis for clarity.

in the excess chemical potential and may partially explain why water does not permeate this tube. It is clear from the structural similarities of the hydrogen bonding water network shown in Fig. 6 that such effects may be important.

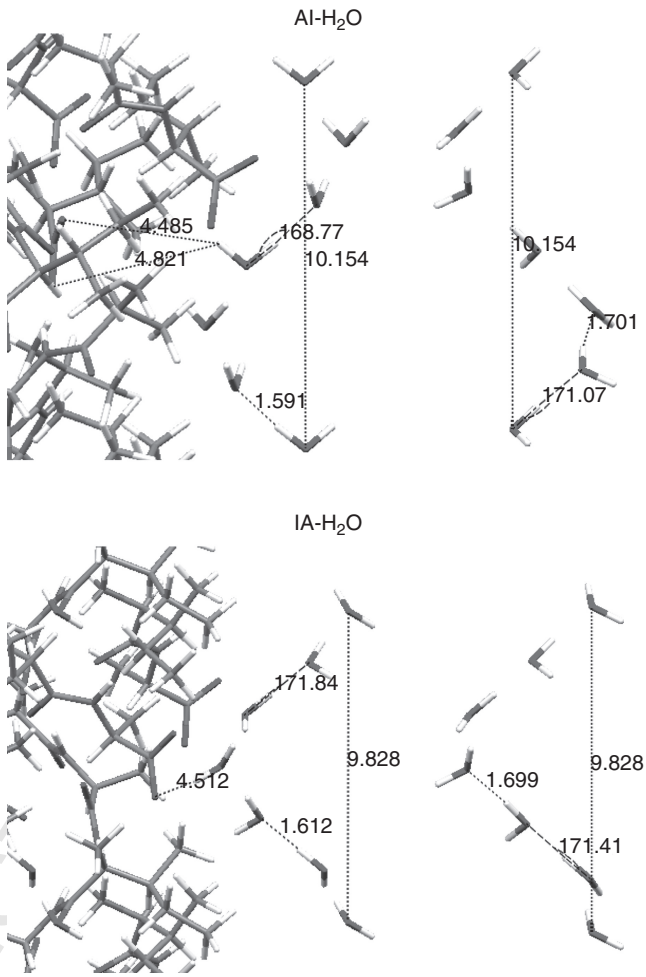

Fig. 6 Theoretical minimum energy structures of AI–H_2O (top) and IA–H_2O (bottom) from DFT. The minimum energy structure of the water helix alone is shown to the right of each.

From both the classical and quantum chemical results, examination of the nuclear motions associated with the THz vibrational normal modes revealed significant participation of the hydrogen bonding network of the nanotube backbone, explaining the high flexibility of the nanotube region for guest molecule permeability. As discussed in more detail elsewhere (Zhang *et al.*, 2008), we find from three-dimensional animations that for many of these modes the side chain motions lead to channel wall deformation (e.g., side chain wagging or channel squeezing motions) but with little change in nanotube volume. However, there were always one or more normal modes associated with a channel-breathing motion

Table I
Results of CHARMM and DFT calculations for the periodic systems of AI and IA with and without H_2O.

	Energy (kJ mol^{-1})				
CHARMM	With H_2O	No H_2O	ΔE^a	H_2O Only	ΔE^b
AI[c]	−3078.2	−2833.2	−245.0	−190.4	−54.64
IA[d]	−3145.0	−2860.2	−289.7	−208.4	−81.38
ΔE	+71.7	+27.0	**+44.7**	**+18.0**	**+26.7**
DFT/PW91					
AI[c]	−4755.6	−4353.7	−401.9	−375.51	−26.40
IA[d]	−4748.5	−4354.2	−394.3	−376.18	−18.11
ΔE	−7.15	+0.46	**−7.61**	**+0.67**	**−8.29**

[a]Differences are specified relative to the dipeptide with water.
[b]Differences are specified relative to the value given in footnote *a*.
[c]X-ray lattice parameters: a=14.2570 Å, c=10.1530 Å for AI.
[d]X-ray lattice parameters: a=14.3720 Å, c=9.8282 Å for IA.

that enlarges the channel capacity significantly (VA was the only exception). For AI, the enhanced coupling of such modes with those of the water helix may further facilitate pathways for guest molecule absorption, substitution and removal.

From the rigorous thermodynamic perspective, The acceptance of water by AI but not IA is directly related to the excess chemical potential compared to bulk water. For a similar system of water in carbon nanotubes (8.1 Å in diameter), estimates of this energy have been reported at the classical level using MD simulations (Hummer *et al.*, 2001). While such classical studies are currently being explored for AI and IA, it is instructive to examine the relative energies of stabilization predicted at the classical and quantum chemical levels. The enthalpies per unit cell are given in Table I. (These energies exclude contributions from the vibrational zero-point energies which are within ±0.8 J mol^{-1} (±0.2 kcal mol^{-1}) for these two systems.) Surprisingly, at the CHARMM level, the stabilization of IA with and without the six water molecules +44.8 kJ mol^{-1} (+10.7 kcal mol^{-1}) greater than the corresponding energy difference predicted for AI (i.e., the dry cell energy differences account for +27 kJ mol^{-1} of the total +71.5 kJ mol^{-1}). Comparison with the relative energies of the water helices by themselves gives some measure of the water-water vs water-nanotube contributions; here +26.8 kJ mol^{-1} of the +44.8 kJ mol^{-1} (6.4 kcal mol^{-1} of the 10.7 kcal mol^{-1}) may be attributed to increased water-tube stabilization and the remaining to increases in the water network itself. Therefore, IA is predicted by CHARMM and the TIP3P water model to be significantly more stable with hydration than AI which is opposite to what is observed.

A similar comparison is given in Table I from the results of quantum chemical calculations. Here, hydration of AI verses IA is slight more favorable by +7.6 kJ mol^{-1} (+1.8 kcal mol^{-1}) with nearly all of increased stability arising from water-tube interactions. This difference per water molecule is small (+1.3 kJ mol^{-1} or

+0.30 kcal mol^{-1}) but comparable to the difference in excess chemical potentials (−3.4 kJ mol^{-1} or −0.82 kcal mol^{-1}) that enables water permeability in carbon nanotubes (Hummer *et al.*, 2001). However, unlike the water/carbon nanotube system, the difference of >4 kJ mol^{-1} per water from CHARMM is unlikely to be overcome by gains in stability from decreased assess to high energy states that dominate the free energy.

A full analysis of the normal modes responsible for the observed THz features including VSCF corrections to the CHARMM frequencies for the hydrated nanotubes will be given elsewhere. We also plan to perform MD simulations to better understand the vastly different permeability dynamics across these different hydrophobic nanotube systems. An attempt to refine these MD simulations will be made based on improving the force field predictions based on the observed THz features.

References

Allen, T. W., Kuyucak, S., and Chung, S. H. (1999). The effect of hydrophobic and hydrophilic channel walls on the structure and diffusion of water and ions. *J. Chem. Phys.* **111,** 7985–7999.

Allis, D. G., Fedor, A. M., Korter, T. M., Bjarnason, J. E., and Brown, E. R. (2007). Assignment of the lowest-lying THz absorption signatures in biotin and lactose monohydrate by sold-state density functional theory. *Chem. Phys. Lett.* **440,** 203–209.

Beckstein, O., and Sansom, M. S. P. (2004). The influence of geometry, surface character, and flexibility on the permeation of ions and water through biological pores. *Phys. Biol.* **1,** 42–52.

Brooks, B. R., Bruccoleri, R. E., Olafson, B. D., States, D. J., Swaminathan, S., and Karplus, M. (1983). CHARMM: A program for macromolecular energy, minimization, and dynamics calculations. *J. Comp. Chem.* **4,** 187–217.

De Groot, B. L., and Grubmuller, H. (2001). Water permeation across biological membranes: Mechanism and dynamics of aquaporin-1 and GlpF. *Science* **294,** 2353–2357.

Delley, B. (1990). An all-electron numerical method for solving the local density functional for polyatomic molecules. *J. Chem. Phys.* **92,** 508.

Delley, B. (2000). From molecules to solids with the $DMol^3$ approach. *J. Chem. Phys.* **113,** 7756.

Ebbinghaus, S., Kim, S. J., Heyden, M., Yu, X., Greubele, M., Leitner, D. M., and Havenith, M. (2008). Protein sequence- and pH-dependent hydration probed by terahertz spectroscopy. *J. Am. Chem. Soc.* **130,** 2374–2375.

Ebbinghaus, S., Kim, S. J., Heyden, M., Yu, X., Heugen, U., Greubele, M., Leitner, D. M., and Havenith, M. (2007). An extended dynamical hydration shell around proteins. *Proc. Natl. Acad. Sci.* **104,** 20749–20752.

Ewald, P. (1921). Die Berechnung opticher und elektrostatischer Gotterpotentiale (Evaluation of optical and electrostatic lattice potentials). *Ann. Phys.* **64,** 253–287.

Görbitz, C. H. (2002). An exceptionally stable peptide nanotube system with flexible pores. *Acta Crystallogr.* **B58,** 849–854.

Gorbitz, C. H. (2003). Nanotubes from hydrophobic dipeptides: Pore size regulation through side chain substitution. *New J. Chem.* **27,** 1789–1793.

Görbitz, C. H., and Gundersen, E. (1996). Valyl Alanine. *Acta Crystallogr. C* **52,** 1764–1767.

Gregurick, S. K., Chaban, G. M., and Gerber, R. B. (2002). Ab initio and improved empirical potentials for the calculation of the anharmonic vibrational states and intramolecular mode coupling of n-methylacetamide. *J. Phys. Chem. A* **106,** 8696–8707.

Gregurick, S. K., Fredj, E., Elber, R., and Gerber, R. B. (1997). Vibrational spectroscopy of peptides and peptide-water cmplexes: Anharmonic coupled-mode calculations. *J. Phys. Chem. B* **101,** 8595–8606.

Gregurick, S. K., Liu, J. H.-Y., Brant, D. A., and Gerber, R. B. (1999). Anharmonic vibrational self-consistent field calculations as an approach to improving force fields for monosaccharides. *J. Phys. Chem. B* **103,** 3476–3488.

Heugen, U., Schwaab, G., Brundermann, E., Heyden, M., Yu, X., Leitner, D. M., and Havenith, M. (2006). Solute-induced retardation of water dynamics probed directly by terahertz spectroscopy. *Proc. Nat. Acad. Sci.* **103,** 12301–12306.

Heyden, M., Brundermann, E., Heugen, U., Niehues, G., Leitner, D. M., and Havenith, M. (2008). Long-range influence of carbohydrates on the salvation dynamics of water—Answers from terahertz absorption measurements and molecular modeling simulations. *J. Am. Chem. Soc.* **130,** 5773–5779.

Hummer, G., Rasaiah, J. C., and Noworyta, J. P. (2001). Water conduction through the hydrophobic channel of a carbon nanotube. *Nature* **414,** 188–190.

Jepsen, P. U., and Clark, S. J. (2007). Precise ab-initio prediction of Terahertz vibrational modes in crystalline systems. *Chem. Phys. Lett.* **442,** 275–280.

Korter, T. M., and Plusquellic, D. F. (2004). Continuous-wave terahertz spectroscopy of biotin: Vibrational anharmonicity in the far-infrared. *Chem. Phys. Lett.* **385,** 45.

Lynden-Bell, R. M., and Rasaiah, J. C. (1996). Mobility and salvation of ions in channels. *J. Chem. Phys.* **105,** 9266–9280.

MacKerell, A. D., Banavali, N., and Foloppe, N. (2000). Development and current status of the CHARMM force field for nucleic acids. *Biopolymers* **56,** 257.

MacKerell, A. D., Jr., Bashford, D., Bellott, M., Dunbrack, R. L., Jr., Evanseck, J. D., Field, M. J., Fischer, S., Gao, J., Guo, H., Ha, S., Joseph-McCarthy, D., Kuchnir, L., *et al.* (1998). All-atom empirical potential for molecular modeling and dynamics studies of proteins. *J. Phys. Chem. B* **102,** 3586–3616.

MacKerell, A. D., Jr., Brooks, B., Brooks, C. L., III, Nilsson, L., Roux, B., Won, Y., and Karplus, M. (1998b). "The Encyclopedia of Computational Chemistry 1." Wiley, Chichester, UK.

Masson, J. B., Sauviat, M. P., Martin, J. L., and Gallot, G. (2006). Ionic contrast terahertz near-field imaging of axonal water fluxes. *Proc. Natl. Acad. Sci.* **103,** 4808–4812.

McIntosh, K. A., Brown, E. R., Nichols, K. B., McMahon, O. B., DiNatale, W. F., and Lyszczarz, T. M. (1995). Terahertz photomixing with diode lasers in low-temperature-grown GaAs. *Appl. Phys. Lett.* **67,** 3844.

Melinger, J. S., Laman, N., Sree Harsha, S., Cheng, S., and Grischkowsky, D. (2007). High-resolution waveguide terahertz spectroscopy of partially oriented organic polycrystalline films. *J. Phys. Chem. A* **111,** 10977–10987.

Melinger, J. S., Laman, N., Sree Harsha, S., and Grischkowsky, D. (2006). Line narrowing of terahertz vibrational modes for organic thin polycrystalline films within a parallel plate waveguide. *Appl. Phys. Lett.* **89,** 251110.

Mendis, R., and Grischkowsky, D. (2001). Undistorted guided-wave propagation of sub-picosecond terahertz pulses. *Opt. Lett.* **26,** 846–848.

Perdew, J. P., and Wang, Y. (1986). Accurate and simple density functional for the electronic exchange energy: Generalized gradient approximation. *Phys. Rev. B* **33,** 8800–8802.

Pine, A. S., Suenram, R. D., Brown, E. R., and McIntosh, K. A. (1996). A terahertz photomixing spectrometer: Application to SO_2 broadening. *J. Mol. Spectro.* **175,** 37.

Plusquellic, D. F., Korter, T. M., Fraser, G. T., Lavrich, R. J., Benck, E. C., Bucher, C. R., Domench, J., and Hight Walker, A. R. (2003). *In* "Terahertz Sensing Technology. Volume 2: Emerging Scientific Applications and Novel Device Concepts" (D. L. Wollard, W. R. Loerop, and M. S. Shur, eds.), Vol. 13(4), pp. 385. World Scientific.

Plusquellic, D. F., Siegrist, K., Heilweil, E., and Esenturk, O. (2007). Applications of THz spectroscopy in biosystems. *Chem. Phys. Chem.* **8**(17), 2412.

Pomes, R., and Roux, B. (1998). Free energy profiles for H+ conduction along hydrogen-bonded chains of water molecules. *Biophys. J.* **75,** 33–40.

Preston, G. M., Carroll, T. P., Guggino, W. B., and Agre, P. (1992). Appearance of water channels in Xenopus oocytes expressing red cell CHIP28 protein. *Science* **256,** 385–387.

Sansom, M. S. P., Smith, G. R., Adcock, C., and Biggin, P. C. (1997). The dielectric properties of water within model transbilayer pores. *Biophys. J.* **73,** 2404–2415.

Siegrist, K., Bucher, C. R., Mandelbaum, I., Hight-Walker, A., Balu, A. R. R., Gregurick, R. S. K., and Plusquellic, D. F. (2006). High resolution Terahertz spectroscopy of crystalline trialanine: Extreme sensitivity to β-sheet structure and cocrystallized water. *J. Am. Chem. Soc.* **128,** 5764–5775.

Verghese, S, McIntosh, K. A., Jackson, A., Gossard, A. C., and Matsuura, S. (2001). Accurate modeling of dual dipole and slot elements used with photomixers for coherent terahertz output power. *IEEE Trans. Microwave Theory Tech.* **49,** 1032.

Whitmire, S. E., Wolpert, D., Markelz, A. G., Hillebrecht, J. R., Galan, J., and Birge, R. R. (2003). Protein flexibility and conformational state: A comparison of collective vibrational modes of wild-type and D96N bacteriorhodopsin. *Biophys. J.* **85,** 1269–1277.

Wilson, E. B., Jr., Decius, J. C., and Cross, P. C. (1955). "Molecular vibrations: The theory of Infrared and raman vibrational spectra." McGraw-Hill, New York.

Zhang, H., Siegrist, K., Plusquellic, D. F., and Gregurick, S. K. (2008). Terahertz spectra and normal mode analysis of the crystalline VA class dipeptide nanotubes. *J. Am. Chem. Soc. In press.*

Disclaimer

Certain commercial equipment, instruments, or materials are identified in this paper to adequately specify the experimental procedure. In no case does identification imply recommendation or endorsement by NIST, nor does it imply that the materials or equipment identified are necessarily the best available for the purpose.